Performance Evaluation of a GLRT Moving Target Detector for TerraSAR-X Along-Track Interferometric Data

Alessandra Budillon, *Member, IEEE*, and Gilda Schirinzi

Abstract—The availability of high-resolution along-track interferometric synthetic aperture radar (ATI-SAR) data with large coverage, such as TerraSAR-X (TSX) data, motivates spaceborne ground moving target detection as an attractive alternative to conventional traffic data acquisition. In this paper, a performance analysis of ground moving targets detection by means of ATI-SAR systems and using a statistical approach is carried out on both simulated and real data. A Gaussian clutter model and a deterministic target response have been assumed. The receiver operating characteristic for the likelihood ratio test (LRT), which can be assumed as a reference best performance case, has been expressed in closed form and has been related to the deflection values, which can be exploited for assessing the improvements in the detection probability with a constant false-alarm rate. For practical applications, the performance of a generalized LRT (GLRT) has been investigated. The analysis carried out on simulated data revealed that the detection results achieved using a GLRT based on a deterministic target model are comparable with those obtained using a GLRT based on a Gaussian target model and are not significantly worse than the theoretical performance of the LRT. Finally, ground moving target detection results on TSX real data are showed.

Index Terms—Along-track interferometry (ATI), detection, generalized likelihood ratio test (GLRT), ground moving target, likelihood ratio test (LRT), synthetic aperture radar (SAR).

I. INTRODUCTION

ALONG-TRACK interferometric synthetic aperture radar (ATI-SAR) systems are multichannel systems capable of detecting moving targets on the ground surface and of estimating their radial velocity [1]–[4]. They can be a powerful tool for wide-area traffic monitoring in all-weather conditions during day and night, even if the limitations related to the revisiting time and to the strong dependence on roads orientations have to be considered. ATI-SAR systems were originally applied to estimate ocean surface currents velocity [5]–[7], showing a very high estimation accuracy, even for low velocity values. In [8], the first analysis of surface current fields derived from ATI TerraSAR-X (TSX) data has been conducted, showing results basically consistent with theoretical expectations.

The recent availability of high-resolution spaceborne SAR data with large coverage, such as TSX and RADARSAT-2 data, has allowed to obtain different experimental examples of traffic monitoring from space [1], [9]. It is well known that the effect of the radial velocity component of a moving target consists in shifting its image along the azimuth direction and in introducing an interferometric phase (ATI phase), depending on the radial velocity value and on the SAR antenna baselines. The azimuth displacement is proportional to the target radial velocity and to the distance from the SAR antenna to the observed ground [2], then for satellite systems, it can amount to a large number of pixels (e.g., in the TSX case, a radial velocity of 50 km/h will produce a displacement of about 1.2 km).

The presence of the ATI phase related to the target velocity suggests the idea of developing proper algorithms for detecting moving targets and estimating their radial velocity using the ATI phase [1]–[4], [9]–[16] or the displaced phase-center antenna (DPCA) method [10], [17]. ATI detectors are considered clutter limited: the smaller the signal-to-clutter ratio (*SCR*), the more likely the target will become buried within the clutter. DPCA detectors, instead, are considered noise limited: the higher the noise, the worse the detection of the slowly moving targets. Anyway, these two approaches apply on SAR processed images, after range and azimuth compression and consequently benefit of a signal-to-noise ratio (SNR) improvement. Other methods for ground moving target indication (GMTI) use space–time adaptive processing (STAP) techniques [18]–[20] by jointly exploiting multiple parallel digitized receiving channels and several transmitted pulses. Space–time approaches are applied to range-compressed raw data and then can suffer from an SNR loss [20]. In order to overcome this problem and detect targets with low radar cross section (RCS) in [20], a new space–time approach has been proposed, which is denoted as imaging STAP [20]. In [21] and [22], a generalization of DPCA that also exploits multiple virtual receiving channels has been proposed. In both [20] and [21], a statistical approach has been considered; it operates clutter cancellation and use a generalized likelihood ratio test (GLRT), with a deterministic target response, for the detection. Clutter cancellation is performed since in GMTI applications, the presence of clutter can significantly affect the detection performance. In fact, it has to be considered that each pixel of the complex image is resulting from the superposition of the signal backscattered by the moving target and the signal returned by the stationary background. In [20], clutter cancellation is performed in the Doppler

domain, whereas in [21], it is done after SAR compression through the inverse clutter covariance matrix. The approach reported in [22] aims at canceling clutter without using any statistical assumptions, thus obtaining a very robust approach, even if suboptimal under the Gaussian clutter assumption.

The clutter is a problem also in ATI-SAR techniques, since in conjunction with the noise, it can corrupt the interferometric phase [23], but it can be taken into account in the statistical signal model, so that radial velocity estimation and target detection can be performed without operating a preliminary clutter cancellation [12]–[16], which in some cases can be a critical operation. In fact, DPCA and STAP can both suffer from limitations of poor clutter cancellation and target attenuation.

Other moving target detection techniques are based, instead, on the defocusing effect produced by the target azimuth velocity. Vehicles moving in along-track direction appear smeared in azimuth when SAR azimuth focusing is matched to the stationary background. The extent of this defocusing is directly proportional to the along-track velocity, and moving target detection can be performed by estimating its along-track velocity component from multichannel data and compensating the related image defocusing effect [24].

In this paper, we analyze the moving target detection performance of an ATI-SAR multichannel technique using a GLRT and adopting a deterministic model for the target and a Gaussian one for the clutter. It represents a modification of the GLRT presented in [16], which was based on a Gaussian target model. In particular, in [16], it was assumed that the complex amplitude of the (stationary) target is a realization of a zero-mean circularly symmetric complex Gaussian random variable with unknown variance, related to the target RCS. As well known, the estimation of a realization of a random variable can be performed in the framework of a classical estimation theory by treating it as a deterministic unknown parameter if its statistical distribution is not available or exploiting its statistical distribution when it is *a priori* known for increasing the estimation accuracy. When the distribution is partially known (such as in the case of Gaussian probability density function (pdf) with known average value and unknown variance), the use of the target pdf could not lead to performance improvement.

In this paper, we investigate the performance achievable by using a deterministic target model, in terms of probability of detection and false alarm. Anyway, both Gaussian and deterministic models are based on the assumption that the target RCS remains constant in the small time required for the SAR antenna to cover the baseline length [25]. This assumption is also required for accurate SAR image focusing, which assumes the target RCS does not change during the Synthetic Aperture (SA) formation time, which is certainly larger than the time delay between the two interferometric acquisitions. If target RCS changes during the synthetic aperture time interval, a defocusing effect producing a loss in the signal intensity is observed in both the interferometric images.

The approach presented is based on SAR processed images and can be applied to any SAR sensor data, with at least two channels. It does not require explicit clutter cancellation as a separate processing step, since clutter is taken into account in the statistical signal model and assumes a fixed clutter covari-
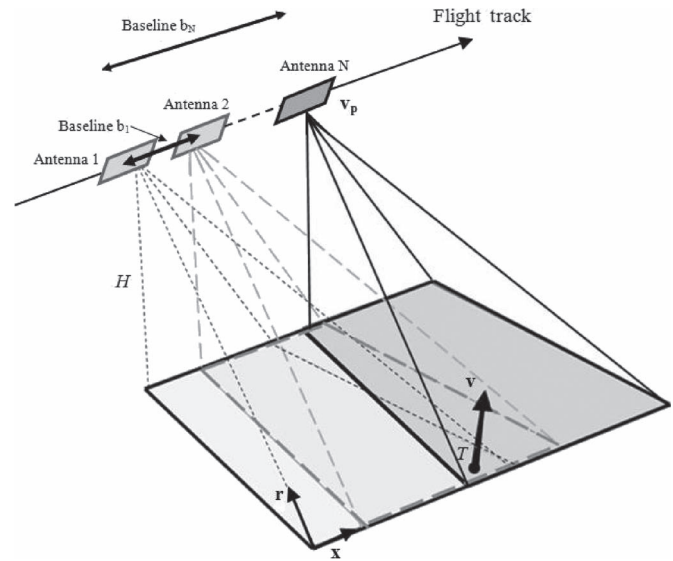

Fig. 1. ATI system geometry.

ance matrix. With the adopted statistical models, the receiver operating characteristic (ROC) associated with the likelihood ratio test (LRT), in the theoretical case of known target parameters (that can be assumed as a best performance reference case), can be expressed in closed form. Moreover, it has been shown that the detection performance is easily related to the deflection of the likelihood ratio pdf. For the case of unknown target parameters, the detection performance obtained by applying a GLRT based on a deterministic target model have proved to be not significantly worse than the LRT one, for sufficiently high radial velocity and *SCR* values. Furthermore, it is shown that the GLRT performance results corresponding to deterministic and Gaussian [16] target models are the same. The validation of the proposed method has been carried out for different target parameters on simulated data and on TSX ATI real data.

II. Multichannel ATI-SAR Signal Model

Here, we introduce the statistical model of the multichannel ATI-SAR signal.

Consider an ATI SAR system consisting of N antennas moving along direction $\mathbf{x}$ (azimuth) and separated along the azimuth by the two-way baselines b_n from the first antenna, with $n = 1, \ldots, N$ and $b_1 = 0$ [3]. Assume $b_n \ll H$, where H is the platform distance from the ground, and a target on the ground moving with a constant velocity $\mathbf{v}_T = v_x \mathbf{x} + v_r \mathbf{r}$, where v_x and v_r are the azimuth and range velocity components, respectively (see Fig. 1).

Let $\mathbf{Z} = [Z_1, Z_2, \ldots, Z_N]^T$, $\mathbf{Z}_C = [Z_{c1}, Z_{c2}, \ldots, Z_{cN}]^T$, $\mathbf{Z}_T = [Z_{T1}, Z_{T2}, \ldots, Z_{TN}]^T$, and $Z_W = [Z_{W1}, Z_{W2}, \ldots, Z_{WN}]^T$, the complex N-dimensional vectors representing the SAR processed images, the stationary ground clutter, the moving target, and the white thermal noise signals, computed in a fixed pixel, where ^{T} stands for the transpose.

The target detection problem can be stated as a hypothesis testing problem, since it can be reduced to the choice between the two statistical hypothesis H_0 and H_1, corresponding to the absence and to the presence of a moving target, respectively.

The SAR image signal can be modeled as

$$\mathbf{Z} = \begin{cases} \mathbf{Z}_C + \mathbf{Z}_W & \text{in absence of a moving target } H_0 \\ \mathbf{Z}_C + \mathbf{Z}_W + \mathbf{Z}_T & \text{in presence of a moving target } H_1. \end{cases}$$

$$(1)$$

The clutter vector $\mathbf{Z}_C$ and the thermal noise vector $\mathbf{Z}_W$ can both be assumed as circularly symmetric complex (or proper complex) Gaussian vectors, with mutually uncorrelated real and imaginary parts, with zero mean and same variance ($\sigma_C^2/2$ and $\sigma_W^2/2$, respectively). While the elements of $\mathbf{Z}_W$ can be assumed uncorrelated, the elements of $\mathbf{Z}_C$ are highly mutually correlated, since they represent clutter image samples taken with the same view angle and with a very short time elapsing between the acquisitions smaller than the time for the synthetic aperture synthesis.

When the moving target is absent (hypothesis H_0, $\mathbf{Z}_T = 0$), the random vector $\mathbf{Z}$ is Gaussian with zero mean and covariance matrix

$$\mathbf{C} = \mathbf{C}_C + \mathbf{C}_W = \sigma_C^2 \begin{bmatrix} 1 & \gamma_{C12} & \cdots & \gamma_{C1N} \\ \gamma_{C12}^* & 1 & \cdots & \gamma_{C2N} \\ \cdots & \cdots & 1 & \cdots \\ \gamma_{C1N}^* & \gamma_{C2N}^* & \cdots & 1 \end{bmatrix} + \sigma_W^2 \mathbf{I}_N$$

$$(2)$$

where * denotes conjugation, $\mathbf{I}_N$ is the N-dimensional identity matrix, $\mathbf{C}_C$ and $\mathbf{C}_W$ are the clutter and noise covariance matrices, and $CNR = \sigma_C^2/\sigma_W^2$ and γ_{Cnm} are the clutter correlation coefficients given by [3]

$$\gamma_{Cnm} = \frac{E\left[Z_{Cn} Z_{Cm}^*\right]}{\sqrt{E\left[|Z_{Cn}|^2\right] E\left[|Z_{Cm}|^2\right]}} = \frac{E\left[Z_{Cn} Z_{Cm}^*\right]}{\sigma_C^2} \quad (3)$$

with $E[\cdot]$ denoting the expected value. We highlight that for circularly symmetric zero-mean Gaussian clutter, the coefficients γ_{Cnm} are real valued and typically assume a value equal to 1 [11], since the stationary clutter signal is acquired by the SAR antennas with the same view angle and with a time delay on the order of a millisecond. In this assumption, it results

$$\mathbf{C} = \sigma_C^2 \left(\mathbf{1}\mathbf{1}^T + \frac{1}{CNR}\mathbf{I}_N \right) \quad (4)$$

where vector $\mathbf{1}$ is the all ones N-dimensional column vector.

As far as the target model is concerned, while in [16], a Gaussian model was assumed, we consider here a deterministic target contribution. The detection performance achieved will be compared with those obtained with the detector presented in [16]. The deterministic model considered here is applicable to the case of a target whose RCS does not change in the small time required to the SAR antenna to cover the baseline length [25] and in absence of other information on its *a priori* statistical distribution. If during this time, the target RCS changes, a defocusing effect is observed, producing a decrease of the *SCR* value, which produces a loss in the detection performance. In our hypothesis, it can be assumed that the target contribution takes the same value A in all the acquired images, which can be considered as a deterministic unknown parameter influencing the *SCR* and the acquired data statistical distribution. Then, the

moving target signal can be modeled as a deterministic vector whose elements can be written as

$$z_{Tn} = Ae^{j\varphi_n} \qquad n = 1, \ldots, N \quad (5)$$

where A is the complex target reflectivity image (with amplitude $|A|$ and phase φ_A) acquired by the nth antenna in the stationary case (zero radial velocity value), not depending on n, and φ_n is a phase related to the target radial velocity through the relation [3]

$$\varphi_n = \left\langle a_n \frac{v_r}{|v_p|} \right\rangle_{2\pi} \qquad n = 1, \ldots, N \quad (6)$$

where $a_n = 4\pi b_n/\lambda$, with λ the operating wavelength, v_p the flying platform velocity, and $<\cdot>_{2\pi}$ the "modulo-2π" operation.

By introducing vector $\boldsymbol{\phi}$

$$\boldsymbol{\phi} = \left[e^{j\varphi_1}, \ldots, e^{j\varphi_N}\right]^T \quad (7)$$

vector $\mathbf{z}_T$ can be written

$$\mathbf{z}_T = \boldsymbol{\phi}|A|e^{j\varphi_A}. \quad (8)$$

In this assumption, the random vector $\mathbf{Z}$ in the hypothesis H_1 is a circularly symmetric Gaussian complex vector with the same covariance matrix as in the hypothesis H_0, and mean different from zero and equal to $\mathbf{z}_T$, and the *SCR* is given by $SCR = |A|^2/\sigma_c^2$.

We note that the adopted model assumptions are simplifying and not necessarily always valid:

1) Gaussian clutter model has been validated over natural scenes [26], such as agricultural and suburban areas, but breaks down over more heterogeneous scenes such as urban areas [4];
2) clutter correlation is not satisfied if longer baselines and/or clutter scenarios with internal motion (as sea clutter) are considered [5]–[8];
3) correlation coefficients are equal to 1 and target amplitude is the same across n only in the ideal case of a perfectly calibrated multichannel radar.

III. STATISTICAL TEST FOR MOVING TARGET DETECTION

As shown in Section II, the pdf of an image pixel depends on the target parameters, which are essentially its complex amplitude A and the target radial velocity. Then, for applying a statistical test for moving target detection, such as the classical LRT [27], these parameters should be known. On a practical level these parameters are unknown, then a suboptimal test, such as the GLRT [27], has to be applied. The GLRT replaces the unknown parameters by their maximum-likelihood (ML) estimates.

Here, we first consider the theoretical ideal case of known target parameters and analyze LRT, to obtain best performance results to be used as reference.

1) Known Target Parameters: Assuming that the target parameters φ_A, v_r, and *SCR* are known, the LRT detector is

$$\Lambda(\mathbf{Z}) = \frac{f(\mathbf{Z}; \varphi_A, v_r, SCR \,|\, H_1)}{f(\mathbf{Z} \,|\, H_0)} \underset{H_1}{\overset{H_0}{\gtrless}} \eta \quad (9)$$

where $f(\mathbf{Z}; \varphi_A, v_r, SCR | H_1)$ and $f(\mathbf{Z} | H_0)$ are the likelihood functions in the statistical hypothesis H_1 and H_0, respectively and η is a threshold that can be determined fixing a probability of false alarm (CFAR).

In the considered assumptions, we have (10), as shown at the bottom of the page.

In (9) and (10) the dependence on φ_A, v_r, and SCR has been highlighted in the target signal $\mathbf{z}_T$, but in the following, it will be omitted.

Taking the natural logarithm, (10) can be written as

$$\Lambda_L(\mathbf{Z}) = \mathrm{Re}\left(\mathbf{z}_T^H \mathbf{C}^{-1} \mathbf{Z}\right) \underset{H_1}{\overset{H_0}{\lessgtr}} \eta' \qquad (11)$$

where

$$\eta' = \frac{1}{2}\left(\ln \eta + \mathbf{z}_T^H \mathbf{C}^{-1} \mathbf{z}_T\right). \qquad (12)$$

The corresponding values of the probability of false alarm P_{FA} and of detection P_D are given by

$$P_{\mathrm{FA}} = \mathrm{Pr}\left\{\Lambda_L(\mathbf{Z}) \geqslant \eta'; H_0\right\} = \int_{\eta'}^{\infty} f_{\Lambda_L}(x; H_0) dx \qquad (13)$$

$$P_D = \mathrm{Pr}\left\{\Lambda_L(\mathbf{Z}) \geqslant \eta'; H_1\right\} = \int_{\eta'}^{\infty} f_{\Lambda_L}(x; H_1) dx. \qquad (14)$$

Then, for computing P_{FA} and P_D, f_{Λ_L} the statistical distribution of Λ_L, in both hypothesis H_0 and H_1, has to be evaluated.

We note that $\mathbf{z}_T^H \mathbf{C}^{-1} \mathbf{Z}$ is a complex Gaussian random variable with mean value equal to zero in the hypothesis H_0 and equal to $\mathbf{z}_T^H \mathbf{C}^{-1} \mathbf{z}_T$ (that is a real value), in the hypothesis H_1, and variance σ^2, given by

$$\sigma^2 = E\left[\left|\mathbf{z}_T^H \mathbf{C}^{-1} \mathbf{Z}\right|^2\right] = E\left[\mathbf{z}_T^H \mathbf{C}^{-1} \mathbf{Z} \left(\mathbf{z}_T^H \mathbf{C}^{-1} \mathbf{Z}\right)^H\right]$$

$$= \mathbf{z}_T^H \mathbf{C}^{-1} \mathbf{z}_T. \qquad (15)$$

Note that σ^2 does not change in the hypothesis H_0 and H_1, since vector $\mathbf{Z}$ in (15) in the two different hypothesis has the same variance but a different average value.

Thus, the variable $\Lambda_L(\mathbf{Z}) = \mathrm{Re}(\mathbf{z}_T^H \mathbf{C}^{-1} \mathbf{Z})$ is still a Gaussian random variable with

$$E[\Lambda_L(\mathbf{Z})] = \begin{cases} 0 & \text{in hypotesis } H_0 \\ \sigma^2 & \text{in hypotesis } H_1 \end{cases} \qquad (16)$$

$$VAR[\Lambda_L(\mathbf{Z})] = \frac{\sigma^2}{2} \text{ in hypotesis } H_0 \text{ and } H_1. \qquad (17)$$

We notice that for evaluating $\mathbf{C}^{-1}$, we can apply the lemma in [28] since $\mathbf{C}$ is a matrix sum of a nonsingular matrix (as

happens in our case due to the presence of thermal noise) and a rank one matrix [see (2)], thus resulting [15]:

$$\mathbf{C}^{-1} = \frac{1}{\sigma_C^2}\left(CNR\mathbf{I}_N - \frac{CNR^2}{1 + N\,CNR}\mathbf{1}\mathbf{1}^T\right) \qquad (18)$$

where $\mathbf{1}$ is an all one N-dimensional vector. Substituting (18) in (15), we obtain

$$\sigma^2 = N \cdot SCR \cdot CNR - SCR\frac{CNR^2}{1 + N\,CNR}\left|\sum_{n=1}^{N} e^{j\varphi_n}\right|^2. \qquad (19)$$

Exploiting (13), the P_{FA} can be easily evaluated in closed form

$$P_{\mathrm{FA}} = Q\left(\frac{\sqrt{2}\eta'}{\sigma}\right) \qquad (20)$$

where Q is the tail probability of the standard normal distribution.

From (20), the threshold η' corresponding to a given P_{FA} is

$$\eta' = \frac{\sigma}{\sqrt{2}}Q^{-1}\left(P_{\mathrm{FA}}\right). \qquad (21)$$

The corresponding probability of detection P_D is given by

$$P_D = Q\left(\frac{\sqrt{2}\left(\eta' - \sigma^2\right)}{\sigma}\right) = Q\left(Q^{-1}\left(P_{\mathrm{FA}}\right) - \sqrt{2}\sigma\right). \qquad (22)$$

Equation (22) represents the ROC of the LRT for a deterministic target model.

Since LRT is optimal in the Neyman–Pearson sense, (22) can be used as a reference for assessing the performance of other tests.

In Fig. 2, we report the ROC given by (22) (solid line) for three different values of SCR (3, 5, and 7 dB), for a target with a radial velocity of 50 km/h and for an ATI-SAR system with one baseline. In particular, we consider TSX parameters. We refer to the TSX dual receive antenna (DRA) mode [29], where the ATI is obtained with an antenna separation of half the total antenna length of 4.8 m and an effective baseline of half the antenna separation, i.e., 1.2 m (platform velocity of 7600 m/s and working frequency of 9.65 GHz). We notice that, for the considered velocity value, for SCR larger than 5 dB, the detection performance is very good, whereas it worsen noticeably for $SCR = 3$ dB.

In Fig. 2, we also show the ROC of the LRT detector for DPCA [17] (dashed line), obtained with the deterministic target model and with the same parameters previously considered. We observe that the ATI detector outperforms the DPCA detector for low SCR, whereas the difference decreases when the SCR increases. In Fig. 3, the ROCs obtained with SCR = 3 dB and for different velocity values are shown. It can be noted that,

$$\Lambda(\mathbf{Z}) = \frac{\frac{1}{\pi^N |\mathbf{C}|} \exp\left\{-\left(\mathbf{Z} - \mathbf{z}_T(\varphi_A, v_r, SCR)\right)^H \mathbf{C}^{-1} \left(\mathbf{Z} - \mathbf{z}_T(\varphi_A, v_r, SCR)\right)\right\}}{\frac{1}{\pi^N |\mathbf{C}|} \exp\left\{-\mathbf{Z}^H \mathbf{C}^{-1} \mathbf{Z}\right\}} \qquad (10)$$
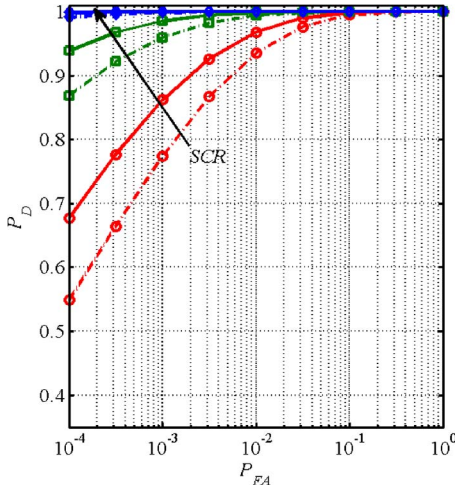
Fig. 2. ROC (P_D and P_{FA} in log scale) obtained with the proposed LRT-ATI detector (solid line) and with the LRT-DPCA detector (point dashed line), for target radial velocity $v_r = 50$ km/h, $CNR = 10$ dB, and SCR values of 3 dB (red circle), 5 dB (green square), and 7 dB (blue diamond) and with one baseline $b = 1.2$ m.
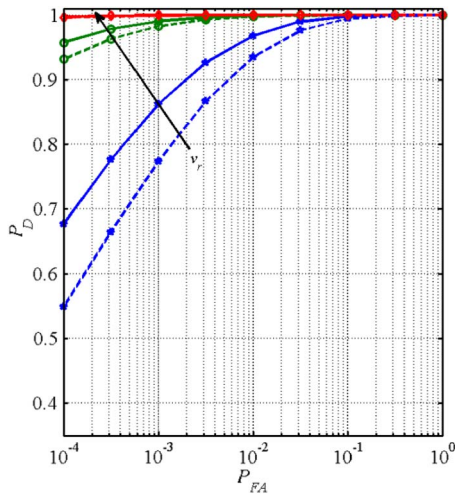

Fig. 3. ROC (P_D and P_{FA} in log scale) obtained with the LRT (solid line) of the proposed LRT-ATI detector (solid line) and with the LRT-DPCA detector (dashed line), for target radial velocity $v_r = 50$ km/h (blue star), 70 km/h, (green circle), 90 km/h (red diamond), $CNR = 10$ dB, and $SCR = 3$ dB, (v_r increases going from the bottom to the top) and with one baseline $b = 1.2$ m.

when velocity increases, the DPCA detector approaches the ATI one; as expected, DPCA is not well suited to detect slow targets.

In order to better investigate the optimal detection performance, we introduce the deflection associated to Λ_L, defined as [30], i.e.,

$$D_{\Lambda_L} = \frac{(E[\Lambda_L(\mathbf{Z})|H_1] - E[\Lambda_L(\mathbf{Z})|H_0])^2}{VAR[\Lambda_L(\mathbf{Z})|H_0]} = 2\sigma^2. \quad (23)$$

Exploiting (22) and (23), we can express P_D as a function of the deflection and of the P_{FA}

$$P_D = Q\left(Q^{-1}(P_{FA}) - \sqrt{D_{\Lambda_L}}\right). \quad (24)$$

Equation (24) shows that, as stated in [30], the maximization of the P_D for a fixed P_{FA} is equivalent to the maximization of
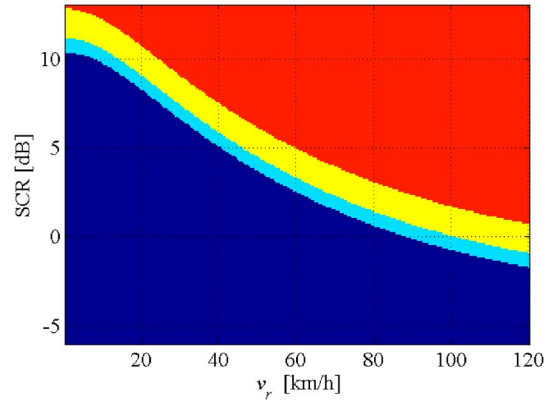

Fig. 4. Areas in the plane $v_r - SCR$, corresponding to the values of the P_D greater than 0.99 (red), between 0.90 and 0.99 (yellow), between 0.80 and 0.90 (cyan), and lower than 0.80 (blue), for an ATI-SAR system with one baseline $b = 1.2$ m and for $CNR = 10$ dB and $P_{FA} = 10^{-4}$, respectively.

the deflection, since Q is a monotonically decreasing function. Note that the detection performance increases with $D_{\Lambda_L} = 2\sigma^2$, which is related to a signal, clutter and noise power ratios as it can be easily seen from (19); thus, the P_D is affected by the amplitude of the target signal and by its radial velocity but not by its phase φ_A.

Equation (24) also shows that for an assigned P_{FA}, a constant P_D is obtained for a constant deflection, which can be obtained with different values of CNR, v_r, SCR, and baseline. If we fix $P_{FA} = 10^{-4}$, we derive the deflection that ensures a determined P_D and then from (19), fixing $CNR = 10$ dB and $b = 1.2$ m, we can find the values of v_r and SCR giving the same deflection value. We show in Fig. 4 the areas of the $v_r - SCR$ plane corresponding to the values of P_D greater than 0.99 (red), between 0.90 and 0.99 (yellow), between 0.80 and 0.90 (cyan), and lower than 0.80 (blue), respectively, obtained considered the TSX ATI-SAR system parameters. We note that in order to detect a slow target with a 99% probability, we need an SCR higher than 12 dB, whereas for faster targets the requested SCR decreases.

Performance can be highly improved using more than one baseline. The same ROC curves shown in Fig. 2 can be also obtained with lower SCR values by considering a hypothetical three antenna ATI-SAR system with the two baselines $b_1 = 1.2$ m and $b_2 = 3.1$ m. In this case, the same deflection values obtained in the previously considered case of one baseline and for SCR values of 3, 5, and 7 dB can be obtained for SCR values of -3.4, -1.4, and 0.6 dB, as can be observed from Fig. 5.

In Fig. 6, we show the areas of the $v_r - SCR$ plane corresponding to values of P_D greater than 0.99 (red), between 0.90 and 0.99 (yellow), between 0.80 and 0.90 (cyan), and lower than 0.80 (blue), respectively, for an ATI-SAR system with two baselines. In particular, we have considered a SAR system with TSX parameters but with the two baselines $b_1 = 1.2$ m and $b_2 = 3.1$ m. We note that the area corresponding to a P_D greater than 0.99 now is bigger and involves lower SCR values, even for slow moving targets. For example, with one baseline, a target moving at 20 km/h could be detected with a P_D greater than 0.99 only for SCR greater than 11 dB, whereas for the two-baseline case, it is sufficient that an SCR is greater than 6 dB.
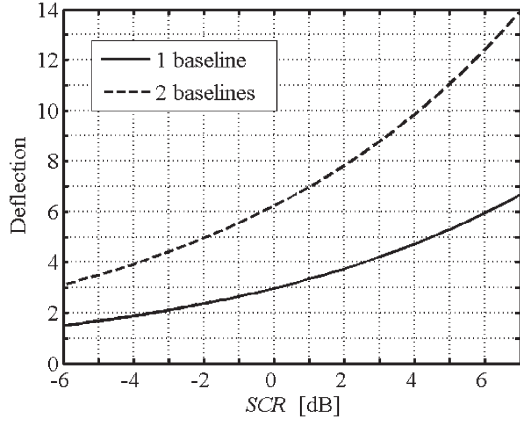
Fig. 5. Deflection versus SCR, for $v_r = 50$ km/h, and $CNR = 10$ dB, for a single-baseline system with $b = 1.2$ m (solid line) and a two-baseline system with $b_1 = 1.2$ m and $b_2 = 3.1$ m (dashed line).
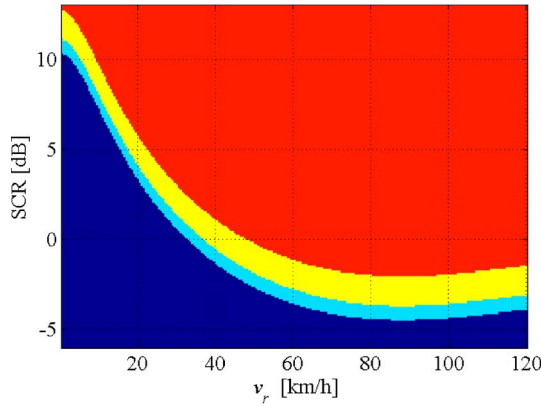

Fig. 6. Areas in the plane $v_r - SCR$, corresponding to the values of the P_D greater than 0.99 (red), between 0.90 and 0.99 (yellow), between 0.80 and 0.90 (cyan), and lower than 0.80 (blue), respectively, for an ATI-SAR system with two baselines $b_1 = 1.2$ m and $b_2 = 3.1$ m, and for $CNR = 10$ dB and $P_{FA} = 10^{-4}$.

However, it has to be reminded that the performance presented is only the best case theoretical performance, since they have been obtained assuming the target parameters to be known. Then, the ROC (22) represents only an upper bound of the expected performance in unknown target parameters case.

2) Unknown Target Parameters: In the more realistic case of unknown target parameters, the GLRT can be applied. It consists in substituting the ML estimates of φ_A, v_r, and SCR in (9), which amounts to performing the following statistical test:

$$\Lambda_G(\mathbf{Z}) = \frac{\max\limits_{SCR \in \Omega_S,\, v_r \in \Omega_v,\, \varphi_A \in \Omega_{\varphi_A}} f(\mathbf{Z}; \varphi_A, v_r, SCR | H_1)}{f(\mathbf{Z} | H_0)} \underset{H_0}{\overset{H_1}{\gtrless}} \delta \quad (25)$$

where the likelihood functions f in the two statistical hypothesis H_1 and H_0 are explicated in (10) and Ω_S, Ω_v, Ω_{φ_A} are the intervals, in which SCR, v_r, and φ_A assume values. Since the ML estimators of SCR, v_r, and φ_A [obtained by maximizing the numerator of (25)] are dependent on the observed data vector, the pdf of $\Lambda_G(\mathbf{Z})$ will differ from the distribution found for the known parameters case.
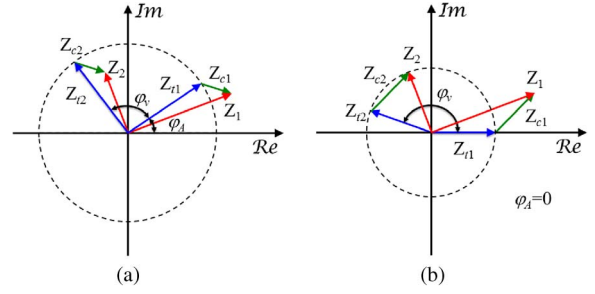

Fig. 7. Phasor diagram of the interferometric signals with the measured data phasors in red, the target phasors in blue and the clutter phasors in green. In (a), the true case and in (b), the case in which it is assumed $\varphi_A = 0$.

It is easy to show that the estimate $\hat{A}$ of the target complex amplitude A, which maximizes the numerator of (25) can be expressed as [31], i.e.,

$$\hat{A} = \frac{\mathbf{z}_T^H \mathbf{C}^{-1} \mathbf{Z}}{\mathbf{z}_T^H \mathbf{C}^{-1} \mathbf{z}_T} \quad (26)$$

where $\mathbf{z}_T$ is depending on v_r and is given by (8). Substituting (26) in (25), the following GLRT test is obtained:

$$\Lambda_G'(\mathbf{Z}) = \max_{v_r \in \Omega_v} \frac{\left| \mathbf{z}_T^H \mathbf{C}^{-1} \mathbf{Z} \right|^2}{\mathbf{z}_T^H \mathbf{C}^{-1} \mathbf{z}_T} \underset{H_0}{\overset{H_1}{\gtrless}} \delta'. \quad (27)$$

Unfortunately, the ML estimator of v_r cannot be expressed in closed form, so that v_r needs to be estimated via an exhaustive search over an interval $(-v_{\mathrm{ramb}}, v_{\mathrm{ramb}})$ with v_{ramb} being the ambiguous radial velocity value equal to $\lambda/4b$. Hence, threshold δ' corresponding to an assigned P_{FA} and the corresponding ROC curve are numerically evaluated by means of a Monte Carlo simulation approach, consisting in simulating a large number of realizations of clutter plus noise signals, i.e., the data under hypothesis H_0. Then, for a given P_{FA}, we evaluated the threshold such that the realizations of the generalized likelihood ratio are greater than it with a probability equal to the fixed P_{FA}. Since we simulated the ROC for a minimum P_{FA} of 10^{-4} we used in all the simulations a sample size of 10^5.

We note that, in this case, the P_D will be affected by the estimation of the three parameters, thus, differently from the LRT case, it now depends also on the estimation of the target phase φ_A. The actual value of φ_A does not influence the velocity estimation accuracy and the GLRT performance, provided that it is properly estimated. For better evidencing the importance of estimating φ_A, we can refer to the phasor representation shown in Fig. 7. In Fig. 7(a), the phasor diagram of the interferometric signals for the case $N = 2$ is shown. The phasors of the measured data $\mathbf{Z}_1$ and $\mathbf{Z}_2$ are represented in red. They are resulting from the sum of the target phasors (in blue) and the clutter phasors (in green). The target phasors exhibit the same amplitude A, the same initial phase offset φ_A, and different phases, due to the radial velocity phase term φ_v. The clutter phasors, instead, due to the very high clutter correlation, are not changing from one acquisition to the other (thermal noise has not been considered, as its effect is equivalent to the production of a negligible change of the clutter phasors that can be neglected for high CNR values). The correct estimation procedure essentially consists in searching the target phasors
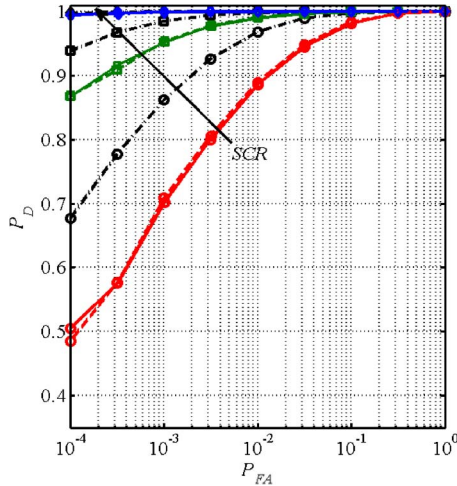
Fig. 8. ROC (P_D and P_{FA} in log scale) obtained with the LRT (point dash black line) and the GLRT for deterministic target model (solid), and with the GLRT for Gaussian target model (dash), for target radial velocity $v_r =$ 50 km/h, $CNR = 10$ dB, and SCR values of 3 dB (red circle), 5 dB (green square), and 7 dB (blue diamond) and with one baseline $b = 1.2$ m.
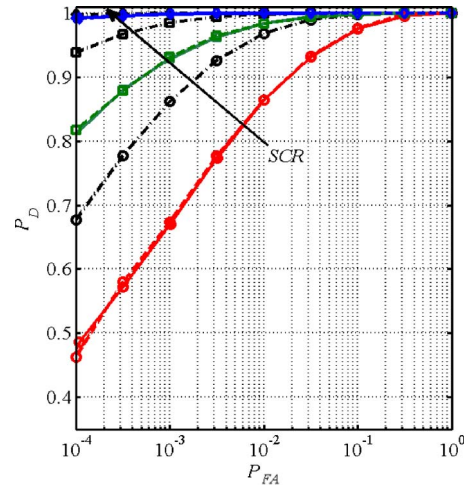

Fig. 9. ROC (P_D and P_{FA} in log scale) obtained with the LRT (point dashed line) and the GLRT for deterministic target model (solid line), and with the GLRT for Gaussian target model (dashed line), for target radial velocity $v_r =$ 50 km/h, $CNR = 10$ dB, and SCR values of -3.4 dB (red circle), -1.4 dB (green square), and 0.6 dB (blue diamond) and with two baselines $b = 1.2$ m and $b_2 = 3.1$ m.

with equal amplitudes, different phases and the same initial phase offset, together with the fully correlated clutter phasors, providing a sum equal to the data phasors. The phasors that would be obtained from an estimation procedure not involving the estimation of the phase offset φ_A and assuming a real-valued target ($\varphi_A = 0$) are shown in Fig. 7(b). As it is evident, the solution obtained by considering $\varphi_A = 0$ is quite different from the real one and leads to a wrong estimate of the phase related to the radial velocity. Anyway, for very high SCR values, when clutter can be neglected respect to the target signal, the velocity estimate becomes independent from the phase φ_A, as expected.

In Fig. 8, we report the comparison between the LRT (point dashed line) and the GLRT (solid line) proposed ATI detectors on simulated data using TSX parameters. We assume a deterministic target model with a velocity value of 50 km/h and for different SCR values (3, 5, and 7 dB), increasing from the bottom to the top. The lowering of the curves in the GLRT case is due to the parameters estimation step, which, as expected, degrades the performance and the degradation decrease for increasing values of SCR. The LRT and the GLRT performance is practically the same for SCR values greater than 7 dB, whereas GRLT exhibits a noticeable loss in detection capability for SCR values lower than 5 dB. In the same figure, we show the behavior, on the same data, of the GLRT (dashed line) detector investigated in [16], which assumes a Gaussian target model. We point out that the two GLRT exhibit experimentally the same performance. A confirmation of that behavior can be found in [32], where following the same model proposed by the authors in [16], it has been shown that the two models provide the same statistical test.

In Fig. 9, we report the comparison between the LRT (point dashed line) and the GLRT (solid line) detectors in the hypothetical case of two baselines ($b_1 = 1.2$ m and $b_2 = 3.1$ m). We assume a deterministic target model and with a velocity value of 50 km/h, but in this case, we consider the three SCR values -3.4, -1.4, and 0.6 dB, which would produce the same

deflection values obtained for the SCR values considered in the single-baseline case of Fig. 8. In this case, the LRT and the GLRT performance is practically the same for SCR values greater than 0.6 dB, whereas GRLT exhibits a noticeable loss in detection capability for SCR values lower than -1.4 dB. In the same figure, we show the behavior, on the same data, of the GLRT (dashed line) detector that assumes a Gaussian target model. It can be observed that also in this case, the two detectors have equivalent performance.

Comparing Fig. 8 with Fig. 9 we note that, while the theoretical LRT performance is the same, since the deflection values in the one-baseline and in the two-baseline cases are the same, GLRT behaves slightly better in the one-baseline case. This behavior is due to the different parameter estimation accuracy values obtained in the two cases, which is not simply related to the deflection value.

In Fig. 10, we report the ROC curves obtained with the LRT of the DPCA detector (point dashed line) and the corresponding GLRT (solid). In addition, for the DPCA, the lowering of the curves in the GLRT case is due to the parameters estimation step, which, as expected, degrades the performance and the degradation decrease for increasing values of SCR.

IV. NUMERICAL AND EXPERIMENTAL RESULTS

To assess the performance of the proposed approach, we present the detection results obtained on simulated and real data.

In order to emphasize the detector performance in the unknown parameters case, we consider a typical situation: a road with ten targets (see Fig. 11) with different SCR and v_r values, according to Table I. The data have been simulated by processing the raw data signal [33] returned by the moving point scatterers superimposed to the signal returned by the stationary Gaussian clutter.

We neglect the defocusing effect due to the along-track velocity, and we consider only the effect of the radial velocity,
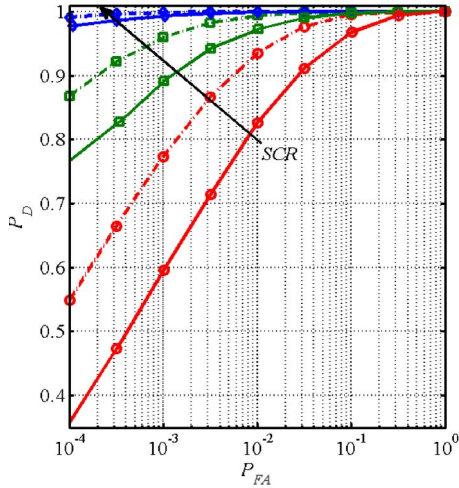
Fig. 10. ROC (P_D and P_{FA} in log scale) obtained with the LRT of a DPCA detector (point dashed line) and the corresponding GLRT (solid), for target radial velocity $v_r = 50$ km/h, $CNR = 10$ dB, and SCR values of 3 dB (red, circle), 5 dB (green, square), and 7 dB (SCR increases going from the bottom to the top) and with one baseline $b = 1.2$ m.
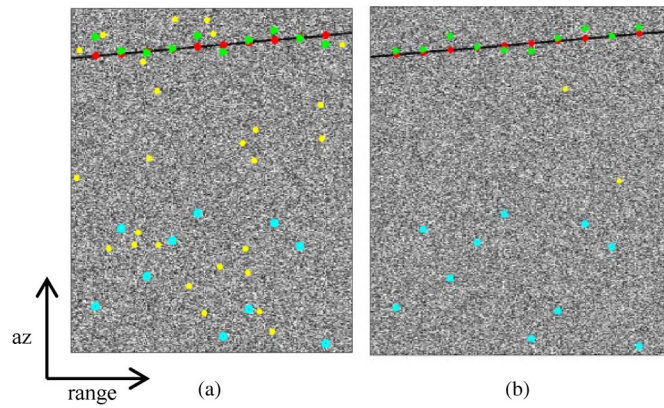

Fig. 12. CRLB$^{1/2}$ (point dash) and RMSE (solid) for target radial velocity v_r from 0 to 150 km/h, $CNR = 10$ dB, and SCR values of 3 dB(red, circle), 5 dB (green, square), and 7 dB (SCR increases going from the top to the bottom) and with one baseline $b = 1.2$ m.

Fig. 11. Detected targets (cyan square), targets displaced in their original position (green triangle), true targets (red circle), and false alarms (yellow star). (a) With $P_{FA} = 10^{-4}$. (b) With $P_{FA} = 10^{-5}$.

TABLE I
TARGET ORIGINAL AND ESTIMATED SCR AND V_R VALUES

SCR dB	Estimated SCR dB	v_r [km/h]	Estimated v_r [km/h]	Repositioning error [m]
9.0	7.2	82.1	88.4	143.3
10.0	10	57.4	58.3	20
7.0	5.2	73.9	73.2	-12.5
8.0	6.2	62.9	63.1	9.2
10.0	9.3	54.7	58.3	82.7
10.0	10.4	95.7	93.2	-55.8
8.0	6.2	87.6	88.4	17.8
7.0	4.5	60.2	63.3	71.9
6.0	3.8	68.4	68.1	-1.7
9.0	8.3	101.2	98.3	-66.6

which produces an azimuth displacement. This does not impair the generality of the results, since the azimuth defocusing effect is equivalent to a decrease of the unknown SCR value.

We consider a system with TSX parameters and simulate a SAR image of 300×1000 pixels along range and azimuth, respectively.

Target detection is performed with the GLRT detector (27) in two cases: with an assigned $P_{FA} = 10^{-4}$ Fig. 11(a) and with
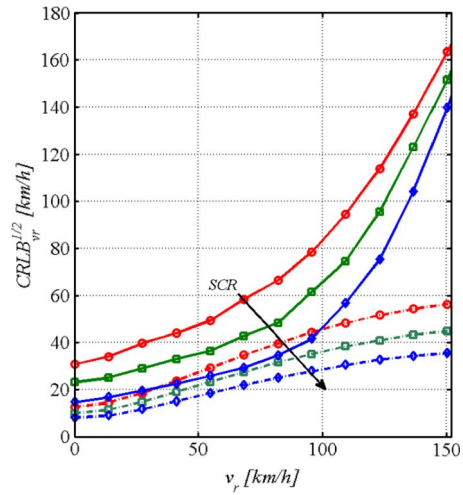
an assigned $P_{FA} = 10^{-5}$ Fig. 11(b). The detected targets are indicated with cyan squares. We see that all the ten moving targets are detected in both cases. The targets moving with radial velocity are shifted in azimuth by Δ_{az} [2]:

$$\Delta_{az} = -R\frac{v_r}{|v_p|} \tag{28}$$

where R is the platform distance from the scene center, and it is related to the height H and the view angle. Consequently, the ten targets are displaced in the azimuth direction (vertical direction) with respect to their true position (red circles). By shifting the azimuth location of the detected targets on the base of (28) using the estimated radial velocity value, the targets appear quite correctly relocated in their real position (green triangle). The false alarms (yellow stars) are 26 for $P_{FA} = 10^{-4}$, and 2 for $P_{FA} = 10^{-5}$, in accordance with the chosen P_{FA}.

In Table I, we report also the original and estimated target SCR and v_r values and the corresponding azimuth repositioning errors, starting from the left in the picture. We observe a quite accurate velocity estimation with a maximum relative error of 7%, the SCR estimation is less accurate, with a maximum relative error of 37%, whereas the highest repositioning error is on the order of 140 m.

In order to better investigate the estimation accuracy, we report in Fig. 12 the Cramer–Rao lower bounds (CRLB) [13] for the radial velocity. In particular, we evaluated the CRLB$^{1/2}$ [km/h] for a range of values of the radial velocity going from 0 to 150 km/h and for different SCR values (3, 5, and 7 dB). We note that, as expected, the CRLBs$^{1/2}$ decrease for increasing values of the SCR, but due to the phase ambiguities, increases approaching the ambiguous radial velocity of 176 km/h. We report also the root-mean-square error (RMSE) that is quite close to the CRLB for low velocity values but explode approaching the ambiguous radial velocity. We note that the estimation error will have an impact on the target repositioning, for example a target with a radial velocity of 50 km/h with TSX parameters have a CRLB$^{1/2}$ of 18 km/h with $SCR = 7$ dB and of 30 km/h with $SCR = 3$ dB (see Fig. 12); thus, it will suffer, on average,
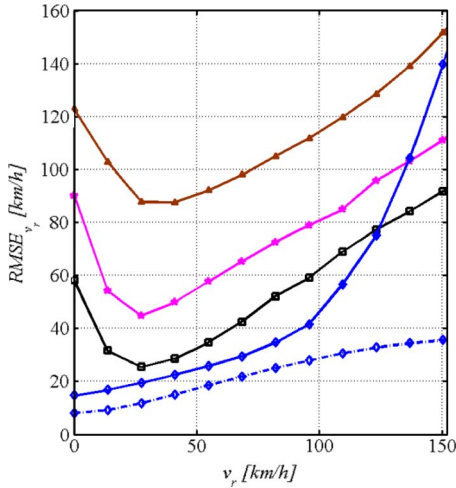
Fig. 13. RMSE (solid) for target radial velocity v_r from 0 to 150 km/h, $CNR = 10$ dB, and $SCR = 7$ dB, in case of the target phase is estimated (blue, diamond), corresponding CRLB $^{1/2}$ (blue, point dash), RMSE in case of the target phase is not estimated and the true φ_A is $\pi/3$ (black, square), $\pi/2$ (pink, star), and π (brown, triangle).
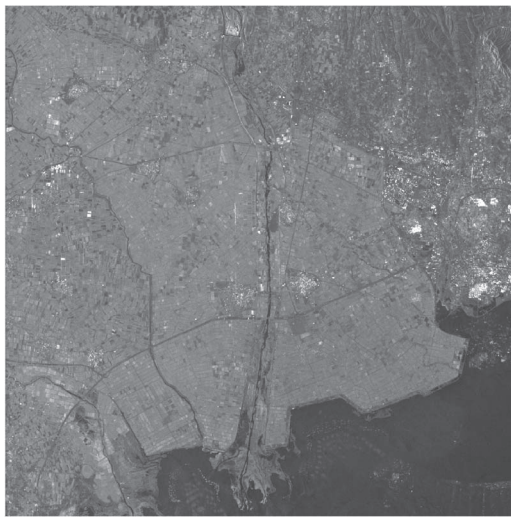

Fig. 14. TSX amplitude image, single look, wide area around Thessaloniki, Greece.

of a repositioning error from 410 m to 680 m. To improve the reposition an additional baseline should be added.

In order to show empirically the effect of not estimating the target phase φ_A we report in Fig. 13 the RMSE in kilometers per hour for a range of values of the radial velocity going from 0 to 150 km/h for $CNR = 10$ dB, and $SCR = 7$ dB. In particular, we note that the RMSE obtained when considering $\varphi_A = 0$ increases for different values of the value of the target phase φ_A ($\pi/3$, $\pi/2$, π). We show also the deviation from the CRLB$^{1/2}$ and the RMSE in the case when the target phase is estimated. Only when approaching the ambiguity velocity value, the estimation errors are comparable. This is reasonable, since the error in that case is related to the phase wrapping.

Finally, we report the results on real data from TSX in DRA mode.

In Figs. 14 and 15, respectively, we show the TSX amplitude image and the subimage of a limited area on which we perform the numerical experiments. In Fig. 16, we reported the esti-
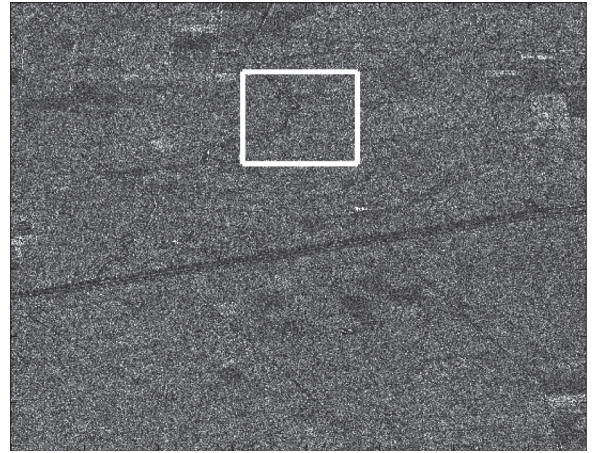

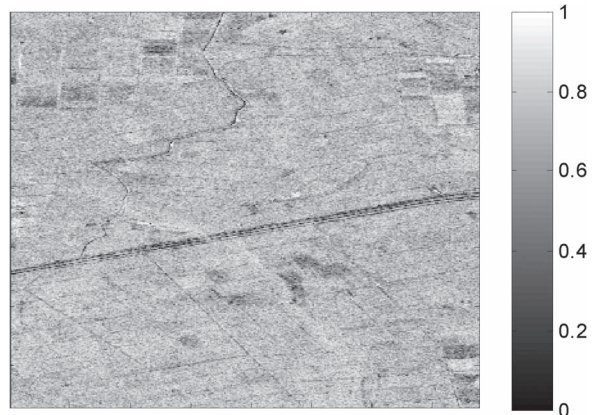Fig. 15. Amplitude subimage of Fig. 13, with the detection area highlighted with a white rectangular.

Fig. 16. Estimated amplitude coherence of the subimage considered.
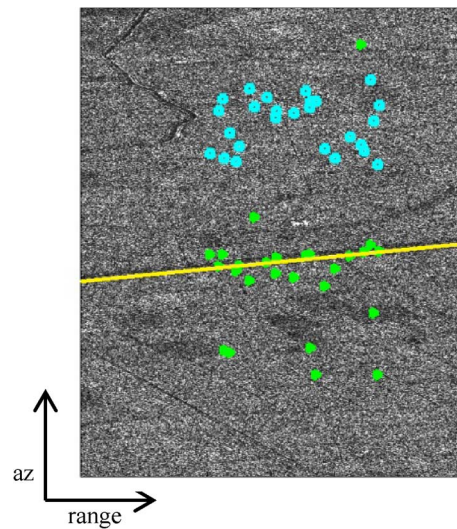

Fig. 17. Detected targets (cyan square) and targets displaced in their original position (green triangle). The principal road is highlighted in yellow.

mated (using a moving window approach) amplitude coherence of the subimage analyzed, we note that the two images are highly correlated. In Fig. 17, we show the detected targets (cyan squares) assuming a P_{FA} equal to 10^{-4}. Since with the TSX parameters, the azimuth shift associated even to a low
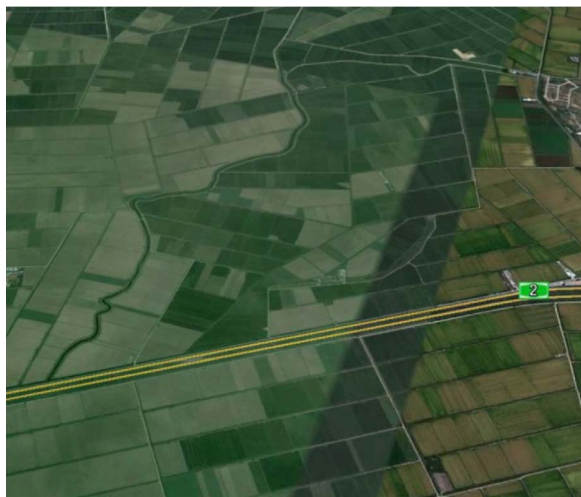
Fig. 18. Subimage area from Google Earth.

TABLE II
DETECTED TARGET ESTIMATED SCR, COHERENCE, AND RADIAL VELOCITY v_R VALUES

SCR [dB]	Coherence	Estimated radial velocity [km/h]
3.3	0.8	55.9
2.6	0.7	86.4
2.3	0.8	86.4
2.9	0.6	106.7
2.1	0.8	121.9
4.7	0.7	60.9
4.2	0.7	66.0
2.9	0.7	106.7
5.2	0.4	60.9
3.0	0.7	91.4
2.2	0.8	86.4
2.4	0.8	81.3
2.6	0.7	91.4
2.8	0.7	91.4
3.0	0.7	81.3
2.1	0.8	137.2
2.2	0.8	152.4
4.2	0.6	76.2
3.1	0.8	60.9
3.5	0.7	66.0
3.5	0.8	55.9
4.8	0.7	55.9
4.0	0.5	91.4
2.5	0.7	106.7
3.2	0.6	116.9
3.7	0.6	81.3

radial velocity value is large (the shift corresponding to a target moving with $v_r = 50$ km/h is in the order of 1.2 km) and the road network is fairly dense in the area considered, so that it is rather difficult to use the road map as *a priori* information for the radial velocity estimation. It can only be exploited in the estimation refinement step. Once the target velocity have been estimated, they can be placed in their original position (green triangle), taking into account the azimuth displacement. As it can be seen, the majority of the targets have been positioned on the roads, in particular we have highlighted in yellow the principal road, a highway, which is also easily visible in the Google Earth image in Fig. 18. In Table II are reported, respectively the estimated *SCR*, coherence and radial velocity of the 26 detected targets. Clutter power and coherence have been empirically evaluated from the data using a moving window approach. We note that the detection area has been chosen of 300×700 pixels and we expected around 21 false alarms with a P_{FA} equal to 10^{-4}, we have filtered 22 targets with a radial velocity lower than 50 km/h since we focused our attention on the traffic flow of the highway. Since the *SCR* are quite low we expect a repositioning error that in some case could be consistent, this is why not all the targets are perfectly repositioned.

V. CONCLUSION

In this paper, we have investigated the detection of ground moving targets using SAR systems, which allow large area coverage in all-weather conditions during day and night. In particular, we refer to multibaseline ATI-SAR systems, whose images exhibit an ATI phase in correspondence of targets moving with a radial velocity. We have investigated a GLRT approach for the target detection, exploiting SAR amplitude and phase of the processed images and assuming a Gaussian clutter model and a deterministic target response.

We have showed that the theoretical detection performance (LRT) in the case of known target parameters can be derived in a closed form. Moreover, the deflection of the pdf of the likelihood ratio can be used in order to assess the theoretical performance achievable for given velocity, target RCS, clutter power level, false alarm rate, and baselines values. In the case

of unknown target parameters, a suboptimal GLRT needs to be used. The performance degrades with respect to the LRT optimal one, due to the parameters estimation inaccuracies, but the degradation is not significant for sufficiently high *SCR* and velocity values. Moreover, we showed on simulated data that the detection results achieved using the GLRT based on a deterministic model for the target response are comparable with the ones obtained using the GLRT based on a Gaussian target model. This behavior is related to the adopted signal model, assuming that only one target realization is present in the multichannel signal, so that the same input information to the parameter estimation and detection procedures is provided for both the considered target models. If, instead, the target complex reflectivity decorrelates along the observation vectors, the two target models are expected to differ and might result in estimation/detection performance differences.

Eventually, experimental results obtained on real TSX ATI data show the capability of the GLRT approach in detecting moving targets for enough high *SCR* and velocity values. The estimation accuracy of the target radial velocity, and consequently, the target azimuth repositioning, is satisfactory for strong and fast targets, but needs improvements for velocity values lower than 50 km/h and low *SCR* values. A noticeable improvement can be reached by using an additional channel (two-baseline systems) or exploiting possible available information on the road maps to refine the target repositioning.

REFERENCES

[1] F. Meyer, S. Hinz, A. Laika, D. Weihing, and R. Bamler, "Performance analysis of the TerraSAR-X traffic monitoring concept," *ISPRS J. Photogramm. Remote Sens.*, vol. 61, no. 61, pp. 225–242, Dec. 2006.

[2] S. Suchandt *et al.*, "Automatic extraction of traffic flows using TerraSAR-X along-track interferometry," *IEEE Trans. Geosci. Remote Sens.*, vol. 38, no. 2, pp. 807–819, Feb. 2010.

[3] A. Budillon, V. Pascazio, and G. Schirinzi, "Estimation of radial velocity of moving targets by along-track interferometric SAR systems," *IEEE Geosci. Remote Sens. Lett.*, vol. 5, no. 3, pp. 349–353, Jul. 2008.

[4] C. H. Gierull, "Moving Target detection with along-track SAR interferometry:A theoretical analysis," Defense Research Development Canada, Ottawa, ON, Canada, Tech. Rep. DRDC-OTTAWA-TR-2002-084, Aug. 2002.

[5] R. M. Goldstein and H. A. Zebker, "Interferometric radar map of ocean surface currents," *Nature*, vol. 328, pp. 707–709, 1987.

[6] R. E. Carande, "Dual baseline and frequency along-track interferometry," in *Proc. IEEE IGARSS*, 1992, pp. 1585–1588.

[7] F. Lombardini, F. Bordoni, F. Gini, and L. Verrazzani, "Multibaseline ATI-SAR for robust ocean surface velocity estimation," *IEEE Trans. Aerosp. Electron. Syst.*, vol. 40, no. 2, pp. 417–433, Apr. 2004.

[8] R. Romeiser, S. Suchandt, H. Runge, U. Steinbrecher, and S. Grünler, "First analysis of TerraSAR-X along-track InSAR-derived current fields," *IEEE Trans. Geosci. Remote Sens.*, vol. 48, no. 2, pp. 820–829, Feb. 2010.

[9] C. H. Gierull, I. C. Sikaneta, and D. Cerutti-Maori, "Two-step detector for RADARSAT-2's experimental GMTI mode," *IEEE Trans. Geosci. Remote Sens.*, vol. 51, no. 1, pp. 436–454, Jan. 2013.

[10] C. H. Gierull, "Statistical analysis of multilook SAR interferograms for CFAR detection of ground moving targets," *IEEE Trans. Geosci. Remote Sens.*, vol. 42, no. 4, pp. 691–701, Apr. 2004.

[11] C. W. Chen, "Performance assessment of along-track interferometry for detecting ground moving targets," in *Proc. IEEE Radar Conf.*, Philadelphia, PA, USA, 2004, pp. 99–104.

[12] N. Stacy and M. Preiss, "ATI slow target detection in a log likelihood framework," in *Proc. EUSAR*, Jun. 2008, pp. 1–4.

[13] A. Budillon, V. Pascazio, and G. Schirinzi, "Joint estimation of moving target reflectivity and velocity via AT-InSAR systems based on complex interferometric data," *ISPRS J. Photogramm. Remote Sens.*, vol. 75, pp. 1–10, Jan. 2013.

[14] A. Budillon, G. Ferraiuolo, V. Pascazio, and G. Schirinzi, "Multi-channel SAR interferometry via classical and Bayesian estimation techniques," *J. Appl. Signal Process.*, vol. 2005, pp. 3180–3193, 2005.

[15] A. Budillon, A. Evangelista, V. Pascazio, and G. Schirinzi, "Multibaseline along track SAR interferometric systems for ground moving target indication," *Proc. IEEE IGARSS*, 2010, pp. 2924–2927.

[16] A. Budillon, A. Evangelista, and G. Schirinzi, "GLRT detection of moving targets via multibaseline along-track interferometric SAR systems," *IEEE Geosci. Remote Sens. Lett.*, vol. 9, no. 3, pp. 348–352, May 2012.

[17] S. Chiu and C. Livingstone, "A comparison of displaced phase centre antenna and along-track interferometry techniques for RADARSAT-2 ground moving target indication," *Can. J. Remote Sens.*, vol. 31, no. 1, pp. 37–51, 2005.

[18] J. H. G. Ender, "Space-time processing for multichannel synthetic aperture radar," *Electron. Commun. Eng. J.*, vol. 11, no. 1, pp. 29–38, Feb. 1999.

[19] D. Cerutti-Maori, C. H. Gierull, and J. H. G. Ender, "Experimental verification of SAR-GMTI improvement through antenna switching," *IEEE Trans. Geosci. Remote Sens.*, vol. 48, no. 4, pp. 2066–2075, Apr. 2010.

[20] D. Cerutti-Maori, I. Sikaneta, and C. H. Gierull, "Optimum SAR/GMTI processing and its application to the radar satellite RADARSAT-2 for traffic monitoring," *IEEE Trans. Geosci. Remote Sens.*, vol. 50, no. 10, pp. 3868–3881, Oct. 2012.

[21] D. Cerutti-Maori and I. Sikaneta, "A generalization of DPCA processing for multichannel SAR/GMTI radars," *IEEE Trans. Geosci. Remote Sens.*, vol. 51, no. 1, pp. 560–572, Jan. 2013.

[22] M. Dragosevic, W. Burwash, and S. Chiu, "Detection and estimation with RADARSAT-2 moving object detection experiment modes," *IEEE Trans. Geosci. Remote Sens.*, vol 50, no. 9, pp. 3527–3543, Sep. 2012.

[23] D. Weihing, S. Hinz, F. Meyer, S. Suchandt, and R. Bamler, "An integral detection scheme for moving object indication in dual-channel high resolution spaceborne SAR data," *Proc. Urban Remote Sens. Joint Event*, 2007, pp. 1–6.

[24] D. Cristallini, D. Pastina, F. Colone, and P. Lombardo, "Efficient detection and imaging of moving targets in SAR images based on chirp scaling," *IEEE Trans. Geosci. Remote Sens.*, vol. 51, no. 4, pp. 2403–2416, Apr. 2013.

[25] G. Palubinskas and H. Runge, "Radar signatures of a passenger car," *IEEE Geosci. Remote Sens. Lett.*, vol. 4, no. 4, pp. 644–648, Oct. 2007.

[26] M. Lucido, F. Meglio, V. Pascazio, and G. Schirinzi, "Closed-form evaluation of the second-order statistical distribution of the interferometric phases in dual-baseline SAR systems," *IEEE Trans. Signal Process.*, vol. 58, no. 3, pp. 1698–1707, Mar. 2010.

[27] S. Kay, *Fundamentals Of Statistical Signal Processing: Detection Theory*, Englewood Cliffs, NJ. USA: Prentice-Hall, 1998.

[28] K. Miller, "On the inverse of the sum of matrices," *Math. Mag.*, vol. 54, no. 2, pp. 67–72, 1981.

[29] M. Gabele *et al.*, "Fore and aft channel reconstruction in the TerraSAR-X dual receive antenna mode," *IEEE Trans. Geosci. Remote Sens.*, vol. 48, no. 2, pp. 795–806, Feb. 2010.

[30] B. Picinbono, "On deflection as a performance criterion in detection," *IEEE Trans. Aerosp. Electron. Syst.*, vol. 31, no. 3, pp. 1072–1081, Jul. 1995.

[31] F. C. Rob, D. R. Fuhrmann, E. J. Kelly, and R. Nitzberg, "A CFAR adaptive matched filter detector," *IEEE Trans. Aerosp. Electron. Syst.*, vol 28, no. 1, pp. 208–216, Jan. 1992.

[32] M. Dragosevic, "GLRT for two moving target models in multi-aperture SAR imagery," in *Proc. IET Radar Conf.*, Oct. 2012, pp. 1–4.

[33] G. Franceschetti, M. Migliaccio, D. Riccio, and G. Schirinzi, "SARAS: A synthetic aperture radar (SAR) raw signal simulator," *IEEE Trans. Geosci. Remote Sens.*, vol. 30, no. 1, pp. 110–123, 123, Jan. 1992.

Alessandra Budillon (M'03) received the "Laurea" degree *(cum laude)* in electronic engineering and the Ph.D. degree in electronic engineering and computer science from the Università degli Studi di Napoli Federico II, Naples, Italy, in 1996 and 1999, respectively.

From January to July 1998, she carried out, within her Ph.D. course of study, as part of her research activity at the Department of Brain and Cognitive Sciences, Massachusetts Institute of Technology, Cambridge, MA, USA. In February 2001, she became an Assistant Professor of telecommunications with the Department of Information Engineering, Seconda Università degli Studi di Napoli, Aversa, Italy. In November 2004, she moved to the Department of Engineering, Università degli Studi di Napoli Parthenope. Her main scientific interests have been focused on statistical signal processing, with applications in data and signals compression and coding, and on remote sensing, with applications in synthetic aperture radar (SAR) processing and SAR interferometry. She has papers published in international journals, she attended several national and international conferences and she is a referee for international journals.

Gilda Schirinzi received the Laurea degree in electronic engineering from the University of Naples "Federico II," Naples, Italy, in 1983.

In the same year, she joined the Department of Electronic Engineering, University of Naples "Federico II," as a Research Fellow. From 1985 to 1986, she was with the European Space Agency, ESTEC, The Netherlands. In 1988, she joined the Istituto di Ricerca per l'Elettromagnetismo e i Componenti Elettronici (IRECE), Italian National Council of Researches (CNR), in Naples. In 1992, she was appointed Head of Electromagnetics Division of IRECE, and in 1997, she became a Senior Researcher. In November 1998, she joined the University of Cassino, Cassino, Italy, as an Associate Professor of telecommunications. In 2005, she became a Full Professor. Since November 2008, she has been with the Telecommunications Group, University of Naples "Parthenope." She has taught signal theory, electrical communications, microwave remote sensing systems, and image processing. Her main scientific interests are in synthetic aperture radar (SAR) signal processing and coding, SAR interferometry, microwave imaging techniques, and image and signal processing for remote sensing applications.